Granular Matter (2022) 24:64
https://doi.org/10.1007/s10035-022-01221-x

BRIEF COMMUNICATION

Geometrical description of impact cratering under microgravity conditions

Cristian Villalobos[1,2] · **Mauricio Housset**[1] · **Germán Varas**[1]

Received: 19 August 2021 / Accepted: 21 February 2022

Abstract
Crater formation has been widely studied through different strategies. One of them simplifies the problem to the impact of a spherical projectile on a granular layer. Due to technical limitations, experimental studies have focused independently on either the corolla formation or the deformation inside the granular bed. Hence, so far, it has not been possible to link these two processes. Here, we present an original experiment that allows us to simultaneously observe the granular dynamics above and below the granular layer in microgravity conditions. The crater morphology is studied considering the dependency on the impact energy, grain size, and shape of the projectile. The results show that this type of experimental configuration makes it possible to quantify the effects of projectile geometry in the crater cavity, something that cannot be captured in traditional tridimensional (3D) deep layer experiments or without the help of advanced imaging techniques such as high-speed X-ray radiography. Finally, this setup opens a new way to study the possible effects of collisions between micrometer-sized dust grains under microgravity conditions, a fundamental process in the early formation of planets in protoplanetary disks.

Keywords Crater formation · Impacts · Free-fall · Microgravity

1 Introduction

Craters are marks of our cosmic past. They are ubiquitous not only on earth but also on the surface of nearly every planet and satellite in the solar system [1]. They can be found in different sizes and shapes, and the process behind their formation can be complex [2]. They are difficult to observe directly, so most of the information collected is taken after the impact in its final state. When the target surface has a negligible cohesive strength (such as sandy soil surfaces of the Earth or lunar regolith), the process is controlled by gravity. This *gravity-limited* regime is characterized by the use of all the energy of the projectile to eject the substrate. In this case, studies have found that the crater diameter (D_c) scales as $D_c \propto E^{1/4}$ [3, 4]. The usual way to study this phenomenon is by releasing a spherical projectile from a fixed height onto a non-cohesive granular target [5]. The morphology of the crater [6, 7], the dependence between its size and the energy of the projectile [4], as well as the relationship between the surface and the corolla [8] have been studied. On the other hand, the evolution of the corolla [9, 10], and its dynamics [11] have also been studied not only by the impact of projectile but also through explosions [12] or local heating produced by a pulsed laser [13]. In these studies, it has been found that the expansion of the corolla (D) follows a power law, $D \propto t^{\gamma}$, where t is the time since impact, and the exponent $\gamma \sim 0.24 - 0.30$. For experiments with deep granular beds, visualization is possible using *X-ray* scanning [14, 15], immersed granular beds [16], or underground cavity collapse [17]. Another important phenomenon related to craters is the low-velocity collisions that occur in planetary rings and protoplanetary disks [18, 19]. In this process, gravity becomes irrelevant, so in order to study them, these conditions must be recreated in a laboratory. Recently, attempts using parabolic flights [20], and a drop tower [21] have been undertaken to create microgravity

✉ Germán Varas
german.varas@pucv.cl
http://fis.ucv.cl/gvaras/

Cristian Villalobos
cristian.villalobos@ug.uchile.cl

[1] Instituto de Física, Pontificia Universidad Católica de Valparaíso (PUCV), Avenida Universidad 330, Valparaíso, Chile

[2] Present Address: Departamento de Física, Facultad de Ciencias Físicas y Matemáticas, Universidad de Chile, Santiago, Chile

Published online: 20 April 2022

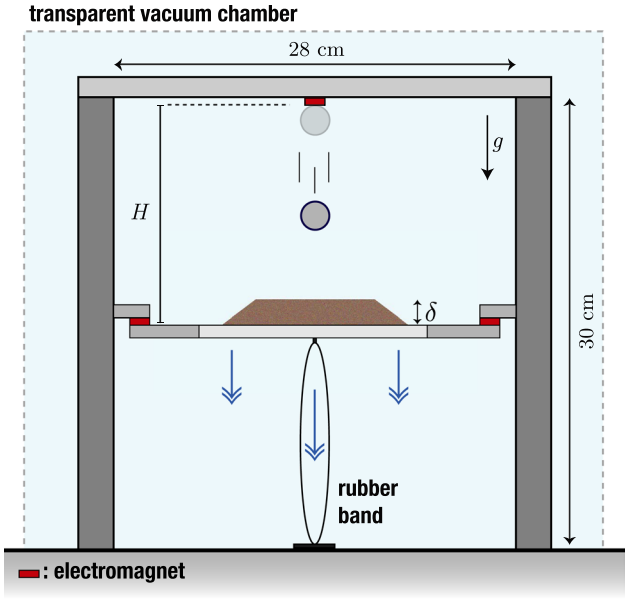

Fig. 1 Experimental setup - A granular disc (height δ) is deposited above a plate fixed by two electromagnets (represented in red). A third electromagnet holds a sphere at a height H from the plate. When the electromagnets are switched off, the sphere starts to fall, and the plate is quickly pulled down by an elastic, leading to the impact of the sphere with the grain layer with a free boundary conditions. The entire system is in a vacuum chamber and air is evacuated up to a pressure P_0 (colour figure online)

environments. However, these studies have focused independently on either the corolla formation or the deformation beneath the granular bed. So far, it has not been possible to observe both processes simultaneously. This study presents a novel experimental setup, which allows us to simultaneously observe the crater cavity and corolla formation with a free boundary condition in a microgravity regime.

2 Experimental setup

The objective of the experimental device is to synchronize the collision of the falling projectile with a granular layer in free fall. For this, the protocol is as follows. A granular layer is formed by depositing glass beads (grain size $d_g = 90-150, 200-300\,\mu$m, and density $\rho_g = 2.5\times10^3$ kg m^{-3}) in a ring of diameter $d = 6.8$ cm and height $\delta = 5$ mm. The ring is then removed, and the granular layer rests over a disk frame held by two electromagnets (Fig. 1). When removing the ring, the grains avalanche towards the sides, forming a trapezoidal shape. A steel sphere (diameter $D_0 = [15, 18, 25, 30]$ mm, and density $\rho_p = 7.8\times10^3$ kg m^{-3}) is held to an electromagnet at the top, at a distance of $H = 10.5$ cm from the plate. When this electromagnet is switched off, the ball begins to fall.

Table 1 Projectiles and granular bed specifications - Two different grains size were used to prepare the granular bed. The characteristic length of the projectiles are the diameter D_0 for the case of spheres or the length of the base (W) for the other geometries. Three versions of conical and pyramidal projectiles were used where the angle (α) with respect to the horizontal was modified while maintaining the same base length

Granular bed grain size (μm)	Projectile geometry	Size (mm) (D_0, W)	Mass (g)
200 – 300	Sphere	15	13.87
	Sphere	18	23.97
	Sphere	25	64.22
	Sphere	30	110.97
90 – 150	Sphere	21	37.70
	Cone	23	38.32
	Pyramide	24	39.97
	Cube	24	41.25

The system is synchronized in order to turn off the two electromagnets holding the plate a few milliseconds before impact. Then, a rubber band violently pulls the frame down, which frees the granular layer. While the granular layer starts to fall under the action of gravity, the sphere hits a layer with a velocity given by $v_p^{\text{teo}} = \sqrt{2g(H-\delta-D_0)} \simeq 1.2$ m/s. Because the impact occurs with both objects in free fall, gravity does not play any role, and the sphere impacts a free granular layer. The setup is fixed inside a cylindrical glass vacuum chamber (30 cm height, 28 cm width), and the air is evacuated up to a pressure $P_0 = [0.6-4.0]$ kPa so as to not disturb the system due to the drastic change in pressure caused when pulling the plate. The dynamic of the collision was followed with a high-speed camera (Phantom Miro M110) recorded at 2000 fps with a spatial resolution of 0.15 mm/px. To obtain the impact of projectiles with different geometries, a hollow volume made in a 3D printer (Zortrax M200, $\rho_T = 1195$ kg/m^3) was glued to a sphere of diameter $D_0 = 21$ mm. In this way, it was possible to maintain the same synchronization system with the electromagnets independent of the projectile geometry. Finally, the two glass beads samples used were intended for two separate purposes (Table 1). On the one hand, the $d_g = 200-300\,\mu$m beads were used only with spherical projectiles to study the evolution of its geometry (Sect. 3.1) and dissipation upon collision (Sect.3.3), while the $d_g = 90-150\,\mu$m beads were used to compare the four types of projectiles (Sect. 3.2).

3 Results

The collision of different projectiles geometries into a free granular layer is shown in Fig. 2. In order to explore the influence of the angle of the conical and pyramidal

projectiles (α) with respect to the horizontal, we constructed three variations for each with $\alpha = 30°, 45°, 60°$ (Sect. 3.2). Since the initial contact, we observe simultaneously the development of the corolla and, after a few milliseconds, the bottom deformation of the granular layer. Qualitatively, both processes are linked, sharing a dependence of their shape with the projectile geometry. The development of the inferior deformation is similar to the one observed in the penetration of granular projectiles into a water target [22]. In their case, since the surface tension of the water is present, the deformation always tends to be circular, whereas in our case, the deformation follows the shape of the projectile. In the same manner, the shape of the corolla differs between the projectiles, where it becomes more evident for polygonal geometries such as the case of the pyramidal projectile and the cube. As the transfer of energy into the horizontal direction depends on the projectile angle α (see the first column in Fig. 2), we observe that the sphere and the pyramid with an angle of $\alpha = 60°$ are more efficient at ejecting the grains than a cube that has an angle of $\alpha = 0°$. In order to quantify the evolution of the impact, we analyze the contour of the corolla and crater produced in the collision through image analysis techniques Fig. 3a. For each data, at least three repetitions were made, and the results presented correspond to the average value between these repetitions.

3.1 Spherical projectile

The results for spheres of different diameters are shown in Fig. 3. First, we quantify the corolla width evolution separated in two parts; (i) The bottom corolla width C_b (Fig. 3b), which accounts for the aperture at the surface of the layer, and (ii) The top corolla width C_t (Fig. 3c), that describes the outer part of the corolla following the evolution of the first grains ejected. Both quantities are not equal, C_t follows the grains that are initially ejected and loose contact with the granular layer, while C_b describes the expansion of the layer produced by the projectile passing through it. In this sense, C_b must start from zero since it describes the evolution of the initial deformation caused by the penetration of the projectile, while C_t can start at a non-zero distance since there is an initial compression of the grains. We found that C_b is well described by a power law $C_b \sim t^{0.3}$, independent of the projectile size (see inset Fig. 3b). The value of the exponent is in agreement with previous observations [12, 13]. In contrast, C_t follows a linear behavior, $C_t = At + 2r_e$, where r_e is the emergence radius defined by Marston et. al. [10], as the horizontal distance from the center of the impact site to the radial location at which the first grains emerge. We found that $2r_e \simeq D_0$ (inset Fig. 3c) which is practically a value slightly lower than found by [10] for granular beds with a packing fraction of $\phi = 0.60$. In their case, the emergence radius was about $2r_e \approx [0.55 - 0.80]D_0$ for glass beads and $2r_e \approx [0.80 - 0.97]D_0$ for sands. The explanation given is due to the fact that the granular bed undergoes a local compaction during the impact. In our case, the granular layer has no boundary conditions; the system cannot be compacted, and hence, our radius of emergence must be close to the actual radius. Additionally, both conditions are not the same as the experiment here presented is in a partial vacuum, and it is known that the velocity of an ejected grain is appreciably reduced by air drag. Regarding the angle evolution of the corolla, we follow its dynamics characterized by fluctuations above an average value and found that $\theta \approx 55° \pm 2°$ is constant in time and independent of the initial energy (Fig. 3d and inset). This angle is defined with respect to the horizontal, considering the initial part of the corolla (Fig. 3a). This method is effective at the beginning of the formation and becomes less efficient as the corolla grows, where it deforms slightly at the top. Again, this corresponds to what is found in the literature [9]. Finally, we quantify the evolution of the aspect ratio of the crater Cr_h/Cr_d (Fig. 3e). The crater grows symmetrically decaying in the same way, independent of the sphere diameter. The bottom radius of the corolla and the crater grow similarly (see inset Fig. 3e). We suspect that a more relevant difference should be observed when increasing the granular bed height (δ) since greater size implies more mass and, therefore, more dissipation. The loss of energy due to collisions would (probably) induce a smaller cavity expansion ($Cr_d < C_b$). It is possible to extend this idea and assume that there is probably a critical height δ_c (proportional to the initial energy) for which no deformation would be observed in the cavity, and the projectile would be completely trapped in the granular layer.

3.2 Different geometries

In order to study the role played by the shape of the projectile, we compare the dependence of the same measured parameters for different projectiles; a pyramid, a cone, a cube, and a sphere (Fig. 4). Additionally we build the pyramid and cone with 3 different angles ($\alpha = 30°, 45°, 60°$), to compare with the cube ($\alpha = 0°$) and the sphere (α not constant between $0° - 90°$). First, C_b has a similar power-law growth type, $C_b \sim t^{\gamma}$, but now the exponent depends on the geometry (Fig. 4a). We obtain an exponent ranging from $\gamma = [0.25 - 0.42]$ for both pyramid and cone with a linear dependence on the angle (Fig. 4b). Something we did not expect to find is that the exponent of the sphere and the cube are roughly the same $\gamma \approx 0.22$, and for the sphere, it is larger ($\gamma \approx 0.30$) when using larger grains. This sensitivity to the size of the grains is interesting, and for the moment, we still do not have an explanation for this. In the same way, the evolution of C_t, follows the same linear growth again, but unlike what is found with spheres, the emergency radius does not have a good correlation with geometry (Fig. 4c–d).

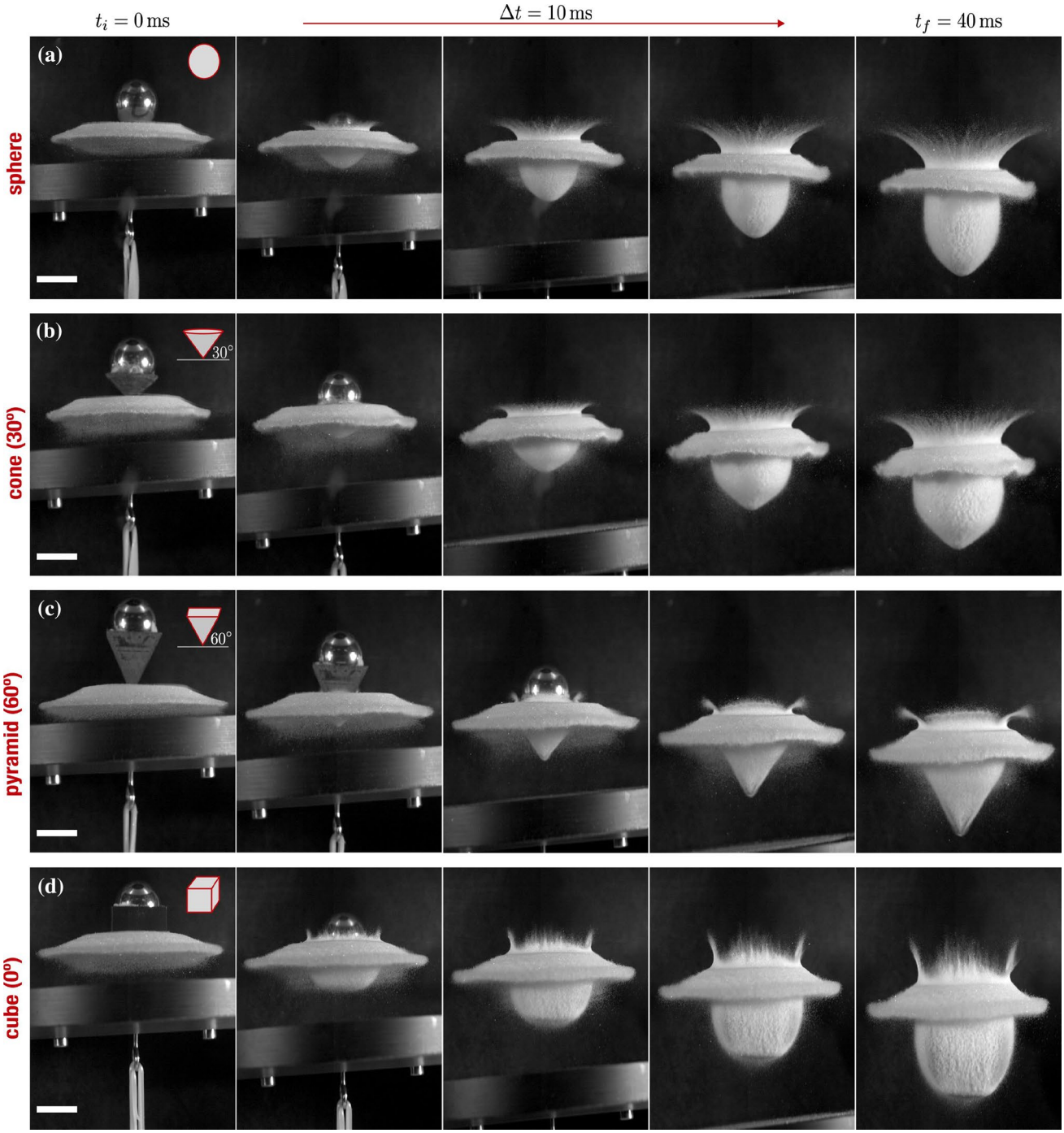

Fig. 2 Snapshots of the collision of projectiles of different geometries ($\Delta t = 10$ ms, grains size $d_g = 90 - 150\ \mu$m, $P_0 = 650$ Pa, scale bar is 20 mm in all the images) - The sequence shows the formation of a corolla followed by the formation of a crater for a **a** sphere, **b** cone ($\alpha = 30°$), **c** pyramid ($\alpha = 60°$) and **d** cube ($\alpha = 0°$). Depending on the geometry, it is observed how the grains curtain (corolla) and the shape of the crater follow the geometry of the projectile. The horizontal and vertical reach of the corolla depends on the impactor geometry. For smooth geometries that do not present drastic changes of direction in their shape, such as the sphere and the cone, the corolla is similar. On the contrary, for geometries that present drastic direction changes between their faces (pyramid and cube), the shape is different and will depend on the angle of observation. The impact does not perturb the outer part of the disc

This is especially noticeable when the face of the projectile facing the granular layer is more horizontal (pyramid and cone $\alpha = 30°$, cube $\alpha = 0°$). It is interesting to note that in these cases the values of the emergence radius are greater than 1, something that is not possible to find in spherical projectiles, independent of grain size. As expected, the cube

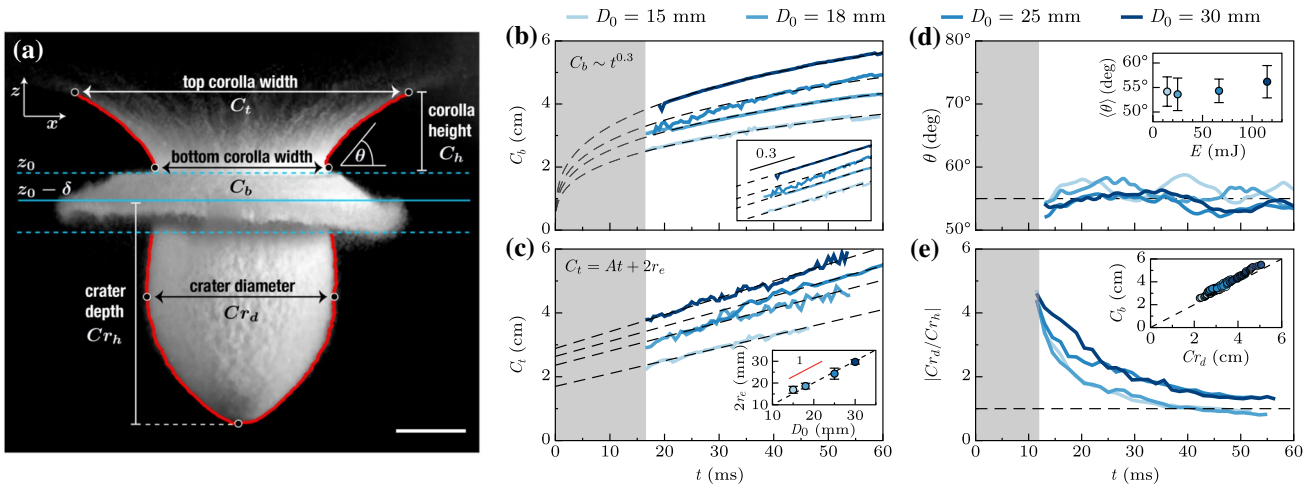

Fig. 3 Image analysis and results - **a** Snapshot of the collision of a sphere with the granular layer ($D_0 = 15$ mm, $d_g = 90 - 150\,\mu$m, $\Delta t = 40$ ms, $\delta = 5$ mm, $P_0 = 4$ kPa, scale bar is 20 mm) and the contour detected through image analysis (red line). The blue dashed lines delimited the zone where the image analysis cannot be performed. (**b**–**e**) $d_g = 200 - 300\,\mu$m, $\delta = 5$ mm, $P_0 = 4$ kPa). **b** Bottom corolla width C_b. The results are well described by a power law $C_b \sim t^{0.3}$ (see inset). **c** Top corolla width C_t. The data follows a linear behavior $C_t = At + 2r_e$ width an offset proportional to the sphere diameter $2r_e \simeq D_0$ ($2r_e/D_0 = 1.0062$) (see inset). **d** Evolution of the corolla angle as a function of time. The inset shows the average value for different sphere diameters. All angles are the same regardless of the initial energy. **e** Crater aspect ratio Cr_d/Cr_h. In all figures, the grey area corresponds to the time where, due to spatial and temporal limitation no data can be found (colour figure online)

is the least efficient on spreading the grains out ($\alpha = 0°$), forming almost a perfect vertical curtain. The corolla height C_h is well fitted by the vertical component of the projectile motion $C_h = tv_p \sin\alpha$, where v_p is the instantaneous velocity of the projectile at the impact. We use $\alpha = 55°$ for the sphere (as the results found previously) (Fig. 4e). The last quantity analyzed is the shape of the crater, which closely follows the geometry of the projectile (Fig. 4f). The similarities are best when the geometry of the projectile has a constant angle (pyramid, cone). In the case of the sphere and the cube, the shape adopted is close to the initial geometry but is lost towards the edges.

3.3 Dissipation

Finally, we quantify the dissipation produced in the collision for the spherical projectiles. For this, we follow the trajectory of the top of the sphere before (v_p) and after (v_p') the collision [Fig. 5a). Both trajectories are subsequently fitted by a quadratic function where the only free parameter is the initial velocity v_{z0} (Fig. 5b). In this way, we get the instantaneous velocity at the moment of contact. For the case of the lower crater deformation (v_g'), we repeat the procedure, but measuring the velocity 10 milliseconds after the impact (see second column Fig. 2). These data are summarized in Table 2. It is important to note that we systematically find that the experimental values are slightly higher than those calculated theoretically. On the one hand, the error between them is small for most

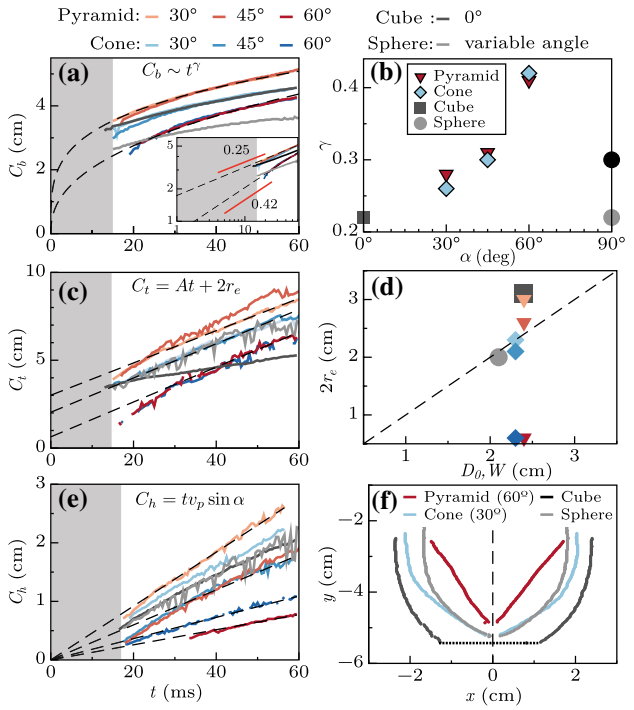

Fig. 4 Projectile geometries ($d_g = 90 - 150\,\mu$m, $P_0 = 650$ Pa) - **a** Bottom corolla width C_b. The results follow a power law $C_b \sim t^\gamma$ with an exponent that depends on the geometry (see inset). **b** Exponent γ as a function of the projectile angle α. The black circle corresponds to exponent found for the impact of the sphere with grains of diameter $d_g = 200 - 300\,\mu$m. For the sake of clarity, the values of the spheres were positioned around $\alpha \approx 90°$. **c** Top corolla width C_t. The data are adjusted by a linear function. **d** Offset comparison with the length of the projectile base D_0, W. **e** Corolla height C_h. **f** Crater contour at $\Delta t = 40$ ms for the different geometries

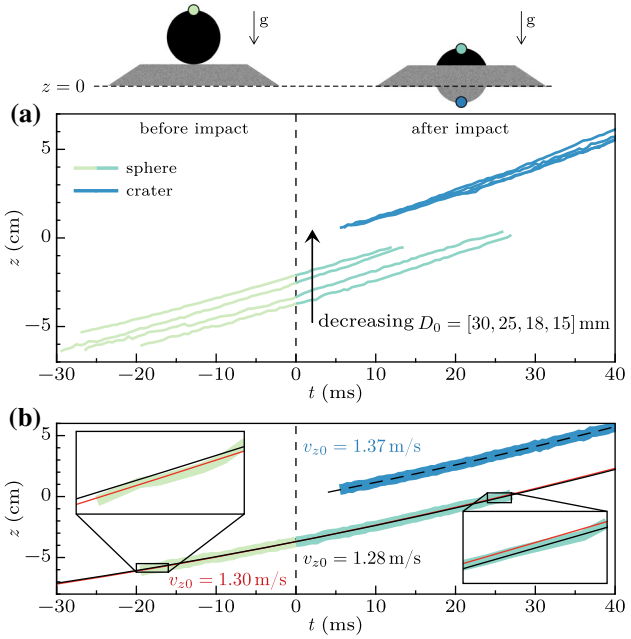

Fig. 5 Spherical projectile and cavity trajectory – **a** vertical motion of the top of the spherical projectile and cavity of the crater ($d_g = 200 - 300\,\mu$m, $\delta = 5$ mm). The data are for four different diameters and the colors indicate the position followed over time. **b** Trajectory analysis for the sphere $D_0 = 30$ mm before and after impact. Before (after) the impact we find a value of $v_p = v_{z0} \approx 1.30$ m/s ($v'_p = v_{z0} \approx 1.28$ m/s). These curves are represented by the red and black line respectively. The deformation of the cavity occurs a few milliseconds later with an initial velocity of $v'_g = v_{z0} \approx 1.37$ m/s (dashed black line) (colour figure online)

cases ($\sim 5\%$), but we must consider that the synchronization between the magnets is not perfect. This sometimes causes the granular bed to start falling a few milliseconds before the impact. Consequently, it increases the distance between the sphere and the grain layer and, therefore, the projectile velocity.

The coefficient of restitution ε can be calculated directly from the relationship between the relative velocities before and after impact,

$$\varepsilon = \frac{\Delta v'}{\Delta v} = \frac{v'_p - v'_g}{v_p - v_g}. \tag{1}$$

Considering that the velocity of the grain layer before impact is zero ($v_g = 0$), we find a range of restitution coefficient $\varepsilon = [0.04 - 0.08]$, equivalent to an inelastic collision in which part of the kinetic energy is dissipated. The total kinetic energy transferred can be calculated by the ratio,

$$\frac{\Delta E_k^T}{E_k} = \frac{E_k - E'_K}{E_k}, \tag{2}$$

Table 2 Instantaneous velocity of the projectiles before (v_p) and after (v'_p) impact the granular layer. We also add the theoretical velocity (v_p^{teo}) of the projectile at the same instant and the instantaneous velocity of the granular layer (v'_g) after the impact

D_0 (mm)	v_p^{teo} (m/s)	v_p (m/s)	v'_p (m/s)	v'_g (m/s)
15	1.29	1.33	1.29	1.34
18	1.26	1.44	1.41	1.52
25	1.21	1.29	1.26	1.36
30	1.17	1.30	1.28	1.37

where E_k (E'_k) is the kinetic energy before (after) the impact. Considering a loose random packing fraction, $\phi \approx 0.6$ when filling the ring, we found $\Delta E_k^T / \Delta E_k \sim 8\% - 15\%$. This is slightly higher than the reported by Katsuragi, et al. [21] where the authors conclude that the dissipative nature of granular clusters is independent of the mechanical properties of the constituent particles. The latter calculation requires the mass of grains displaced by the sphere (m_g). It is complex to define the effective mass in contact with the sphere. For this purpose, we have considered a cylinder with a diameter equal to the sphere and height similar to the layer of grains. However, small corrections to this value and the packing fraction (which should be smaller because the system is in free fall) cause the dissipation to decrease by at least 10%; therefore, this value should be considered as an upper limit of dissipation.

4 Concluding remarks

We have presented a novel experimental setup which allows the observation of the complete deformation of a granular layer in a microgravity regime with a free boundary condition. To our knowledge, this is the first time that both processes (corolla and cavity) can simultaneously be observed. The formation of the corolla and cavity are followed in time for different shapes. We have quantified the crater growth dynamics which follow a power law similar to those observed in other experiments. However, the exponent depends sensibly on the geometry of the projectile. For our projectiles, which have the same initial energy but different shape, we find a range of $\gamma = [0.22 - 0.42]$. The role of projectile geometry in the shape of the corolla remains to be understood. A recent research shows the sensitivity of the corolla to small deformations in the projectile [23] which could explain the differences found in our results between the pyramidal projectile and the cone for the same angle. One solution could be to place a complementary camera at the bottom (or top) of the experiment that would allow quantifying the evolution of the crater (or corolla) for geometries that have drastic changes between their faces (e.g.,

polygons). At the present moment, the setup restricts the exploration for higher distances. In the near future, we plan to modify the setup and begin the study for a greater range of energies and the possibility of changing the boundary conditions and increasing the layer height. We believe that these two quantities will provide better detail on how the growth and crater form will evolve.

Finally, this experimental device opens a new way to study crater formation in microgravity conditions. It is also an opportunity to explore emerging topics such as the formation of planets in protoplanetary disks [19]. In this sense, it is important to notice that many aspects of planet formation (like particle collision) are needed to be performed in a laboratory under microgravity conditions as a complement to simulations and theory. For example, tribocharging is one ingredient that promotes tiny dust particles in protoplanetary disks to aggregate into ever-larger bodies in the millimeter range. A promising opportunity would be to complement our device with a system capable of measuring individual particle charges during free fall as proposed by Waitukaitis and Jaeger [24].

Acknowledgements The authors thanks Menka Stojanova for the initial help with the image detection program. We also thank Valérie Vidal and Nicolás Mujica for discussion and a proofreading of the article. G.Varas acknowledge financial support from PUCV DI Regular Project No. 039.438/2017.

Declarations

Conflict of interest The authors declare that they have no conflict of interest.

References

1. Melosh, H.J.: Impact cratering: A geologic process. Oxford University Press, New York (1989)
2. H. Katsuragi, *Physics of Soft Impact and Cratering* (Springer Japan, 2016)
3. Amato, J., Williams, R.: Crater formation in the laboratory: an introductory experiment in error analysis. Am. J. Phys. **66**, 141 (1998)
4. Uehara, J.S., Ambroso, M.A., Ojha, R.P., Durian, D.J.: Low-speed impact craters in loose granular media. Phys. Rev. Lett. **90**(19), 194301 (2003)
5. Cook, M.A., Mortensen, K.S.: Impact cratering in granular materials. J. Appl. Phys. **38**, 5125 (1967)
6. Walsh, A.M., Holloway, K.E., Habdas, P., de Bruyn, J.R.: Morphology and scaling of impact craters in granular media. Phys. Rev. Lett. **91**(10), 104301 (2003)
7. Simon, J., de Bruyn, J.R.: Shape of impact craters in granular media. Phys. Rev. E **76**(4), 041306 (2007)
8. Sabuwala, T., Butcher, C., Gioia, G., Chakraborty, P.: Ray systems in granular cratering. Phys. Rev. Lett. **120**(26), 264501 (2018)
9. Deboeuf, S., Gondret, P., Rabaud, M.: Dynamics of grain ejection by sphere impact on a granular bed. Phys. Rev. E **79**(4), 041306 (2009)
10. Marston, J.O., Li, E.Q., Thoroddsen, S.T.: Evolution of fluidlike granular ejecta generated by sphere impact. J. Fluid. Mech. **704**, 5 (2012)
11. Boudet, J., Amarouchene, Y., Kellay, H.: Dynamics of impact cratering in shallow sand layers. Phys. Rev. Lett. **96**(15), 158001 (2006)
12. Pacheco-Vázquez, F., Tacumá, A., Marston, J.O.: Craters produced by explosions in a granular medium. Phys. Rev. E **96**(3), 032904 (2017)
13. Marston, J.O., Pacheco-Vázquez, F.: Millimetric granular craters from pulsed laser ablation. Phys. Rev. E **99**, 030901 (2019)
14. Royer, J.R., Corwin, E.I., Flior, A., Cordero, M.L., Rivers, M.L., Eng, P.J., Jaeger, H.M.: Formation of granular jets observed by high-speed X-ray radiography. Nat. Phys. **1**(3), 164 (2005)
15. Homan, T., Mudde, R., Lohse, D., van der Meer, D.: High-speed X-ray imaging of a ball impacting on loose sand. J. Fluid. Mech. **777**, 690 (2015)
16. Varas, G., Vidal, V., Géminard, J.C.: Dynamics of crater formations in immersed granular materials. Phys. Rev. E **79**(2), 021301 (2009)
17. Loranca-Ramos, F.E., Carrillo-Estrada, J.L., Pacheco-Vázquez, F.: Craters and granular jets generated by underground cavity collapse. Phys. Rev. Lett. **115**(2), 028001 (2015)
18. Blum, J.: Dust evolution in protoplanetary discs and the formation of planetesimals. Space Sci. Rev. **214**(2), 1–9 (2018)
19. Wurm, G., Teiser, J.: Understanding planet formation using microgravity experiments. Nat. Rev. Phys. **3**(6), 405 (2021)
20. Colwell, J.E., Sture, S., Cintala, M., Durda, D., Hendrix, A., Goudie, T., Curtis, D., Ashcom, D.J., Kanter, M., Keohane, T., Lemos, A., Lupton, M., Route, M.: Ejecta from impacts at 0.2-2.3 m/s in low gravity. Icarus **195**(2), 908 (2008)
21. Katsuragi, H., Blum, J.: Impact-induced energy transfer and dissipation in granular clusters under microgravity conditions. Phys. Rev. Lett. **121**(20), 208001 (2018)
22. González-Gutiérrez, J., Carrillo-Estrada, J., Ruiz-Suárez, J.: Penetration of granular projectiles into a water target. Sci. Rep. **4**, 6762 (2014)
23. Pacheco-Vázquez, F.: Ray systems and craters generated by the impact of nonspherical projectiles. Phys. Rev. Lett. **122**, 164501 (2019)
24. Waitukaitis, S.R., Jaeger, H.M.: In situ granular charge measurement by free-fall videography. Rev. Sci. Inst. **84**(2), 025104 (2013)